LANGMUIR Article
Cite This: *Langmuir* 2019, 35, 2209–2220 pubs.acs.org/Langmuir

Probing the Colloidal Particle Dynamics in Drying Sessile Droplets

Karam Nashwan Al-Milaji and Hong Zhao*

Department of Mechanical and Nuclear Engineering, Virginia Commonwealth University, BioTech One, 800 East Leigh Street, Richmond, Virginia 23219, United States

Supporting Information

ABSTRACT: Particle deposition and assembly in the vicinity of contact lines of evaporative sessile droplets have been intensively investigated during the past decade. Yet little is known about particle arrangement in the contact-line region initiated by the self-assembled particles at the air–liquid interface and how the particle pinning behaves differently compared with that when particles are transported from the bulk of the sessile droplet to the three-phase contact line. We utilized the dual-droplet inkjet printing process to elucidate the versatility in particle deposition and assembly generated near the contact-line region and demonstrated the influence of such printing technique on particle pinning at the contact line after solvent evaporation. Wetting droplets containing sulfate-functionalized polystyrene (sulfate-PS) nanoparticles were jetted over the supporting droplets with carboxyl-PS nanoparticles, where the interplay between the solvent evaporation and particle transport dictates the final morphology of particle deposition. Depending on the particle size and concentration used in the supporting droplet, different morphologies of particle depositions near the periphery of the supporting droplet have been obtained such as stratified rings, blended rings, and rings of particles mainly from the air–liquid interface. Three characteristic times are considered in this study, namely, total time for solvent evaporation (t_{evp}), time required for the colloidal particles in the supporting droplet to reach the contact line and form the first layers of deposition (t_{ps}), and time needed for the particles at the interface to reach the contact line (t_{pw}). The ratios of characteristic times (t_{ps}/t_{evp}) and (t_{ps}/t_{pw}) determine the final particle assembly near the contact-line region. The ability to control such particle deposition and assembly could have a direct implication on developing facile, cost-effective technologies essential for patterning heterogeneous structured coatings and devices.

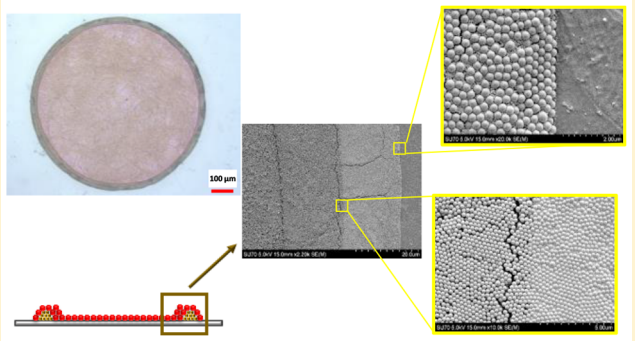

INTRODUCTION

The accumulation and assembly of colloidal particles at the edges of evaporative particle-laden droplets have been intensively studied in the past few decades.[1,2] During the course of solvent evaporation, the colloidal particles are forced to transport to the three-phase contact-line region by virtue of the evaporation-induced flow, especially when no natural convection or Marangoni flow is present.[3,4] Depending on many factors such as particle size,[5] particle shape[6,7] and concentration,[8] particle–particle and particle–substrate interactions,[9,10] substrate wettability and temperature,[11,12] and so on, the transported colloidal particles might deposit near the edge of the sessile droplet, producing the ubiquitous coffee-ring effect.[13] The motif behind such phenomenon is the nonuniform evaporation flux across the curved air–liquid interface of the sessile droplet, where it is found to be higher in vicinity of the three-phase contact line.[14,15] The coffee-ring effect is considered detrimental in printing and coating technologies.[16,17] Nonetheless, it has been exploited in a number of technological applications.[18−20]

In an effort to investigate the behavior of binary particles near the periphery of sessile droplets, Monteux and Lequeux examined the building of colloidal deposition generated at the edge of the evaporative sessile droplet with respect to time.[21] When bidisperse mixtures of colloidal particles were utilized, particle separation phenomena in the vicinity of the contact-line region were identified, where smaller particles always tended to penetrate further into the leading edge of the droplet as opposed to bigger particles.[21] Recently, Noguera-Marín et al. studied the segregation and discrimination of charged particles with different densities during solvent evaporation. Changing substrate wettability and particle charge-mass ratios in low-ionic-strength solutions influenced the segregation of binary colloidal suspensions.[22] The highly negatively charged particles were observed to transport and deposit in the vicinity of the contact line at a faster pace than those with less particle charge density. Additionally, the author identified the strong dependence of particle depositions on the receding contact angle of the substrate, which is directly correlated to the so-called "wedge effect".[22] Such particle arrangement phenomenon near the three-phase contact line has been demonstrated as a feasible solution for sorting out biological entities in sessile

Received: October 9, 2018
Revised: December 14, 2018
Published: January 10, 2019

DOI: 10.1021/acs.langmuir.8b03406
Langmuir 2019, 35, 2209–2220

droplets (e.g., proteins, micro-organisms, and mammalian cells).[23]

In this study, we have investigated the particle pinning in the vicinity of the three-phase contact line formed in conventional sessile droplets and demonstrated an alternative mechanism of particle pinning initiated by the air−liquid interface through implementing the dual-droplet inkjet printing. Confocal microscopy was utilized to directly image the particle transport and pinning. Furthermore, the differences between the two pinning mechanisms were investigated by introducing colloidal particles into both the wetting droplet and the supporting droplet during the dual-droplet printing. Depending on the particle size and concentration, different particle depositions have been obtained in the vicinity of the contact line, such as a ring of particles mainly from the air−liquid interface, blended ring, and stratified ring of particles dispersed in the bulk and particles floating at the interface of the supporting droplet.

Three characteristic times, t_{evp}, t_{ps}, and t_{pw}, which represent the total time for solvent evaporation, time required for colloidal particles in the vicinity of the contact line in the bulk of the supporting droplet to reach and form the first layers at the contact line, and time needed for particles at the interface to reach the contact line, respectively, were calculated and compared to determine the final particle deposition. The characteristic time ratio (t_{ps}/t_{evp}) resembles whether the particles in the bulk of the supporting droplet have sufficient time to reach the contact line before solvent evaporation completes. On the contrary, the characteristic time ratio (t_{ps}/t_{pw}) determines the competition between the particles pinning in the bulk of the supporting droplet and the particles at the interface during solvent evaporation. The ability of controlling such particle deposition and assembly could have a direct implication on developing facile, cost-effective technologies essential for patterning heterogeneous structured devices and coatings.

MATERIALS AND METHODS

Materials. Polyethylene terephthalate (PET) films (MELINEX ST505) with 125 μm thickness were supplied by TEKRA, a Division of EIS. Sulfate latex beads (8% w/v, 300 nm), carboxyl latex beads (4% w/v, 20 nm, 100 nm, 500 nm, and 1 μm), sulfate latex beads (2% solid, 200 nm) with yellow-green fluorescent dye, carboxyl latex beads (2% solid, 20 nm) with a Nile red fluorescent dye, and fluorescein F1300 dye were purchased from Thermo Fisher Scientific. KOPTEC ethanol (99.5% purity) was acquired from VWR. Deionized (DI) water with a resistivity of 18.2 MΩ × cm was produced by Direct-Q water purification system (Millipore Sigma). All chemicals were used as received without further purification.

Confocal Microscopy Characterization. To monitor the particle pinning and deposition at the contact line, confocal laser scanning microscopy (Zeiss, LSM 710) was utilized in this study. A 60× oil lens with a numerical aperture of 1.4 was employed with a working distance of 0.19 mm and a scanning area of 140 μm × 140 μm. The laser scanning microscope (LSM) had a lateral resolution of ∼174 nm (or 184 nm) and a vertical resolution of 498 nm (or 524 nm) based on the 488 nm (or 514 nm) argon laser utilized to excite the fluorescent dyes. Glass slides were used as transparent substrates required for the confocal microscopy. In brief, a coverslip glass slide with 170 μm thickness was rinsed with DI water and dried by nitrogen before use. The measured apparent water contact angle on the coverslip was ∼60 ± 2°.

In the case of scanning the supporting droplet without colloidal particles, a 110 μL droplet of DI water with 0.1 mg/mL concentration of fluorescein F-1300 was dispensed on the coverslip and scanned using the 488 nm argon laser to capture the interface of the supporting droplet. To capture the nanoparticles at the air−liquid interface, a 5 μL suspension containing 200 nm sulfate-PS particles (10 mg/mL particle concentration in ethanol) with yellow-green fluorescent dye was carefully dispensed onto the supporting droplet (containing DI water only) using a microdispenser. The 514 nm laser was utilized to image the nanoparticles at the interface. The interval between the scanned slices was 200 nm in the case of imaging the supporting droplet and the nanoparticle assembly at the air−liquid interface. To avoid the crosstalk between the fluorescent dyes of nanoparticles in the bulk and at the interface of the supporting droplet, a 110 μL droplet of DI water with 0.5 mg/mL concentration of 20 nm carboxyl-PS particles labeled with Nile red was tested separately. The latter was scanned with the 514 nm laser and a 20 nm step size to capture the particle migration from the bulk of the supporting droplet to the contact line.

Ink Preparation. The as-received suspensions of polystyrene particles were ultrasonicated for 5 min to ensure a homogeneous suspension of the nanoparticles. Then, two kinds of inks were prepared to perform the dual-droplet inkjet printing. The as-received carboxyl-PS particles (4% w/v, 20 nm, 100 nm, 500 nm, and 1 μm) were diluted with DI water to obtain colloidal suspensions with particle concentrations of 0.2 and 0.5 mg/mL that were utilized as inks for the supporting droplet. The printing ink for the wetting droplet was prepared by diluting the sulfate-PS particles (8% w/v, 300 nm) with ethanol to obtain a colloidal suspension with a particle concentration of 10 mg/mL that was jetted over the supporting droplet. Each suspension was ultrasonicated for another 5 min before printing.

Dual-Droplet Inkjet Printing Process. The inkjet printing platform (Jetlab 4, MicroFab) consists of four printing stations, two of which were used in this study. Supporting droplets and wetting droplets were jetted from two piezoelectric nozzles with orifice diameters of 80 μm (MJ-ATP-01-80-8MX, MicroFab) driven by a waveform generator (Jetdriver III, MicroFab). In brief, a supporting droplet was generated by jetting multiple bursts of colloidal suspensions of DI water with different sizes of carboxyl-PS particles (a total volume ∼110 nL) on the substrate at a jetting frequency of 500 Hz. Then, wetting droplets containing sulfate-PS nanoparticles were jetted to the center of the supporting droplet using the second 80 μm nozzle at a frequency of 1 Hz. In this work, we have used a jetting speed of ∼1.3 m/s and a droplet volume of ∼550 pL (diameter ≈ 102 μm) for the wetting droplets. This is to ensure spreading of the wetting droplet over the interface of the supporting droplet upon impact. PET films (MELINEX ST505) were used as substrates for the dual-droplet inkjet printing. The apparent water contact angle on a clean PET substrate was ∼70 ± 2°, and the receding angle was ∼44 ± 2°.

Morphology Characterization. An ultra-high-resolution scanning electron microscope (HITACHI SU-70 FE-SEM) with 5 kV and 15 mm scanning distance was used for morphology characterization of the printed patterns. To minimize the charging effect of the PS nanoparticles, the samples were coated with platinum using a platinum sputter (Denton Vacuum Desk V) for 120 s.

Analytical Analysis. In this study, an analytical analysis based on the Hu−Larson model was considered to comprehend the driving mechanism behind the particle deposition and assembly and to predict the characteristic times for particle pinning attained in the contact-line region in the dual-droplet printing process. The characteristic time for two adjacent particles in vicinity of the contact line to meet each other has been proposed and experimentally verified to describe the coffee ring formation.[5] The comparison of the characteristic time for particle pinning to the total evaporation time determines the coffee ring formation.[5,16,26] We have implemented this approach in the dual-droplet printing configuration to evaluate and compare the particle pinning from the interface of the supporting droplet, the particle pinning from the bulk of the supporting droplet, and the total evaporation time.

In the present model, the following assumptions are made: (i) In the bulk of the supporting droplet, the particles are homogeneously dispersed. (ii) The interface of the supporting droplet is uniformly covered with nanoparticles as a result of the spreading of the wetting

DOI: 10.1021/acs.langmuir.8b03406
Langmuir 2019, 35, 2209−2220

droplets over the former one. (iii) The air−liquid interface of the supporting droplet is assumed to be a spherical cap, and the gravitational effect is neglected because the Bond number is $Bo = \frac{\rho g d_0^2}{\sigma} < 0.002$, where ρ is the density of water (note, the ethanol over the interface of the supporting droplet is not considered because its volume fraction is <5% of the entire volume of the supporting droplet even when nine wetting droplets are jetted), g is the gravitational acceleration, d_0 is the inflight diameter of the jetted droplets, and σ is the surface tension. (iv) Solvent evaporation across the interface of the supporting droplet is assumed to be diffusion-limited, and the air−liquid interface is considered to be in phase equilibrium. (v) Particle motions in the bulk and at the interface of the supporting droplet are governed by the diffusion- and evaporation-induced flow approximated at the initial particle concentration.

The time required for the solvent of the supporting droplet to totally evaporate, with a contact angle close to 90° (in this study, θ = 70°), can be approximated by the following equation[24]

$$t_{evp} = f(\theta)\frac{\rho R_{depo}^2}{D(1 - RH)c_v} \tag{1}$$

where $f(\theta) = {}^{2 - 3\cos(\theta) + \cos^3(\theta)}/_{6\sin^3(\theta)}$, R_{depo} is the radius of the supporting droplet deposition, D is the diffusivity of solvent vapor in air, RH is the relative humidity, and c_v is the saturated vapor concentration.

With the assumption that the colloidal nanoparticles in the bulk of the supporting droplet are homogeneously dispersed, the mean distance, L_m, between two colloidal particles is estimated by eq 2[5]

$$L_{m,B} = ({}^{V_0}/_{N_s})^{1/3} \tag{2}$$

where V_0 is the initial volume of the supporting droplet, N_s is the total number of particles in the bulk of the supporting droplet, and the subscript B refers to the bulk of the supporting droplet. On the contrary, the mean distance between two colloidal nanoparticles at the interface of the supporting droplet is estimated by eq 3

$$L_{m,I} = ({}^{S_{cap}}/_{N_w})^{1/2} \tag{3}$$

where S_{cap} stands for the spherical cap surface area of the supporting droplet, N_w is the number of particles in the wetting droplet (therefore at the interface), and the subscript I refers to the interface of the supporting droplet. Bearing this in mind, the diffusion time scale of particles in the bulk and at the interface of the supporting droplet could be evaluated by the Einstein diffusion equation $t_{diff} = {}^{L_m^2}/_{2D_p}$.[25] D_p is the diffusion constant of spherical particles in a liquid flow with low Reynolds numbers, $D_p = k_B T/6\pi\eta R_p$, where k_B is the Boltzmann constant, T is the absolute temperature, η is the dynamic viscosity of the fluid, and R_p is the radius of the colloidal particle. Accordingly, the mean diffusion velocity of colloidal particles in the bulk and at the interface of the supporting droplet can be calculated by eq 4[26]

$$u_{diff} = {}^{k_B T}/_{3\pi\eta L_m R_p} \tag{4}$$

Solvent evaporation across the interface of the supporting droplet is a nonuniform process.[13,14] This, in turn, induces a lateral evaporative flow that entrains the colloidal particles to the contact-line region. The initial radial velocity of the induced capillary flow present in the evaporating supporting droplet can be expressed by eq 5 derived in the Hu−Larson model.[27]

$$u_r = \frac{R_{depo}}{t_{evp}}\left\{\frac{3}{8}\frac{1}{\check{r}}[(1 - \check{r}^2) - (1 - \check{r}^2)^{-\lambda(\theta)}]\left(\frac{z^2}{h^2} - 2\frac{z}{h}\right) + \frac{\check{r}h_0 h}{R_{depo}^2}[J\lambda(\theta)(1 - \check{r}^2)^{-\lambda(\theta)-1} + 1]\left(\frac{z}{h} - \frac{3}{2}\frac{z^2}{h^2}\right)\right\} \tag{5}$$

where $\check{r}$ is a dimensional radius, $z(r)$ and $h(r)$ are the local height in the bulk and the local maximum height at the interface of the supporting droplet, respectively, $\lambda(\theta)$ is a parameter indicating the uniformity of evaporation across the surface of sessile droplets, which could be evaluated by $\lambda(\theta) = {}^1/_2 - {}^\theta/_\pi$, and J is the evaporation flux at $\check{r} = 0$[27]

$$J = ({}^{t_{evp}}/_{\rho h_0})({}^{Dc_v(1 - RH)}/_{R_{depo}})(0.27\theta^2 + 1.3)[0.6381 - 0.2239(\theta - {}^\pi/_4)^2] \tag{6}$$

Particle depositions obtained in the dual-droplet inkjet printing are composed of particles in the bulk and particles at the interface of the supporting droplet, where both the particle motion and solvent evaporation come into play. Particle size and concentration utilized in the system have a significant impact on the particle velocity, u_p, which consists of the diffusion velocity and advection velocity driven by the evaporation-induced flow. In this study, radial velocity is considered as the advection velocity because the particle pinning involves the radial movement of the particles toward the contact line. The particle velocity is expressed as, $u_p = u_{diff} + u_r$, assuming that the particles follow the evaporation-induced flow perfectly.

The radial velocity in eq 5 is evaluated at distance $\check{r}$ near the three-phase contact line of the supporting droplet, where $\check{r} = 1 - {}^{(L_{m,B} + L_{p,B})}/_{R_{depo}}$, and vertical height of ∼10% of the particle diameter lifted from the substrate surface.[5] Herein, $L_{p,B}$ is defined as a finite distance between the initial pinning position of the contact line and the first layer of the outer ring deposition[5]

$$L_{p,B} = {}^{R_p}/_{\tan({}^\theta/_2)} \tag{7}$$

In this model, the characteristic time for the particle in the bulk of the supporting droplet to reach and form the first layers of particles at the contact-line region can be evaluated by $t_{ps} = {}^{L_{m,B}}/_{u_{p,B}}$. Likewise, the radial velocity for the particles at the interface is evaluated at $\check{r} = 1 - {}^{(L_{m,I} + L_{p,I})\cos\theta}/_{R_{depo}}$, where $L_{p,I} = {}^{R_p}/_{\sin\theta}$. The schematics of particles in the contact-line region in the bulk of the supporting droplet and at the interface of the supporting droplet are shown in the Supporting Information (Figure S1). For simplicity, the advection velocity along the interface is taken as the radial velocity multiplied by ${}^1/_{\cos\theta}$. The characteristic time for the particles at the interface to travel toward the substrate and form the first layers of particles at the contact line can be expressed by $t_{pw} = {}^{L_{m,I}}/_{u_{p,I}}$, where the mean distance between two particles in this case is approximated by eq 3. The competition among the characteristic times (i.e., t_{evp}, t_{ps}, and t_{pw}) determines the morphology of particle deposition in the vicinity of the contact line produced at the completion of solvent evaporation.

RESULTS AND DISCUSSION

Particle Pinning and Assembly in Conventional and Dual-Droplet Inkjet Printing. Solvent contact-line pinning of evaporative sessile droplets is an intricate process, which is usually determined by the substrate wetting property through introducing surface roughness[28,29] or chemical heterogeneities.[23,30,31] Nevertheless, the initial pinning on substrates could be enhanced by introducing suspended particles to anchor the contact line.[13] Particle pinning at the contact line is a critical prerequisite condition for the well-known coffee-ring formation, where the colloidal particles migrate to the contact-

DOI: 10.1021/acs.langmuir.8b03406
Langmuir 2019, 35, 2209−2220

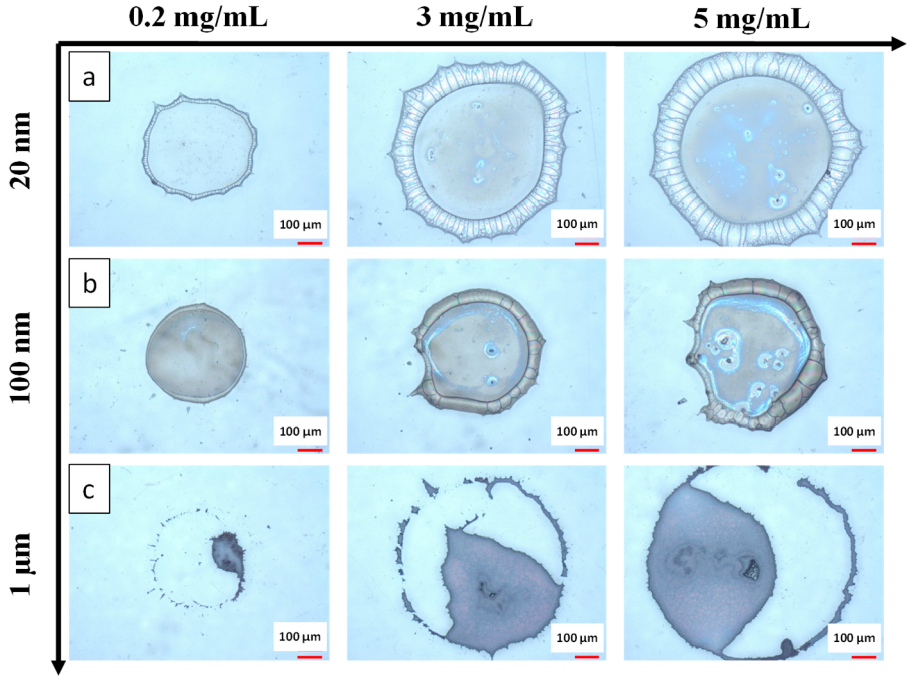

Figure 1. Conventional inkjet printing of particle-laden droplets on the PET substrates: (a) 20 nm carboxyl-PS particles, (b) 100 nm carboxyl-PS particles, and (c) 1 μm carboxyl-PS particles with different particle concentrations. The scale bar is 100 μm.

line region during solvent evaporation. To compare the mechanism of particle pinning at the contact line from particles spread on the interface to that of conventional direct-printing of particle-laden droplets, we first printed colloidal suspensions of carboxyl-PS particles dispersed in DI water on a PET substrate to determine under which condition the particle pinning is achieved. It is worth noting that the water receding angle on the PET substrate is ~44 ± 2°, which is different from the typical requirement of pinned contact lines for the "coffee-ring" formation. This high receding angle also implies that the "wedge effect", that is, the formation of particle depletion zones near the contact line, is insignificant for various sizes of PS particles.[22]

Carboxyl-PS particle-laden droplets of ~110 nL were jetted on the PET substrates. Figure 1 shows the particle assembly with respect to different carboxyl-PS particle sizes and concentrations in the sessile droplets directly printed on the PET substrates. Smaller particles such as 20 and 100 nm tend to consistently migrate with the evaporation-induced flow, where they deposit and form the outermost layers of particle deposition at the three-phase contact line. However, the contact lines obtained from printing colloidal suspensions of 20 nm PS particles with 0.2 and 3 mg/mL particle concentrations depin, followed by a secondary contact-line pinning in a later stage of solvent drying. In conventional inkjet printing of sessile droplets, the particle pinning/depinning behavior at the contact line is governed by forces exerted on colloidal particles in the evaporating sessile droplet such as drag force,[14] van der Waals force,[6,32] electrostatic force,[33] and capillary force.[34] In the early stages of solvent evaporation when the contact lines are initially pinned, the drag force initiated by the outward motion of the evaporation-induced flow is dominant. In this case, the particles are forced to migrate to the rim of the sessile droplet. However, in later stages of solvent drying, capillary forces become dominant, prompting the particles to depin along with the receding contact lines.[35] Capillary forces tend to sweep the particles back toward the center of the supporting droplet, whereas van der Waals and electrostatic attraction between the particles and the substrate tend to lock the particles at the contact-line region.[36] If the particle concentration is low, as shown in Figure 1a,b, then the capillary force dominates the particle–substrate interactions, leading to the particle depinning phenomenon of the initial contact line. However, a secondary pinning line forms where the particles successfully pin along with the new contact line, leading to a coffee-ring formation. This occurs whenever the swept particles along with the particles migrating from the bulk of the sessile droplet toward the contact line have sufficient particle–substrate interactions to cause the secondary contact-line pinning. It should be mentioned that the PET substrate has some surface defects by which the motion of the receded contact lines is somewhat affected.

In contrast, the particles pin at the original contact line when printing colloidal suspension with a higher particle concentration (e.g., 5 mg/mL) using the same particle size. Under this condition, contact-line receding is excluded, and the contact lines remain pinned until the solvent is completely evaporated. Increasing particle loading means more particles are carried to the contact line. This, in turn, increases the particle–substrate van der Waals and electrostatic interactions in the contact-line region, resulting in contact-line pinning.[35] In addition, the evaporation-induced convective flow transports almost all of the nanoparticles to the edge of the sessile droplet, producing a thick ring with several cracks. Crack development is attributed to the strong capillary stresses generated in later stages of solvent evaporation process.[37] This observation of crack formation is consistent with the results reported elsewhere.[38]

Similarly, jetting sessile droplets with 100 nm carboxyl-PS particles gave similar results as the 20 nm particles with regards to the particle pinning at the secondary contact line. Yet the contact lines of the printed deposits depin even though the

DOI: 10.1021/acs.langmuir.8b03406
Langmuir 2019, 35, 2209–2220

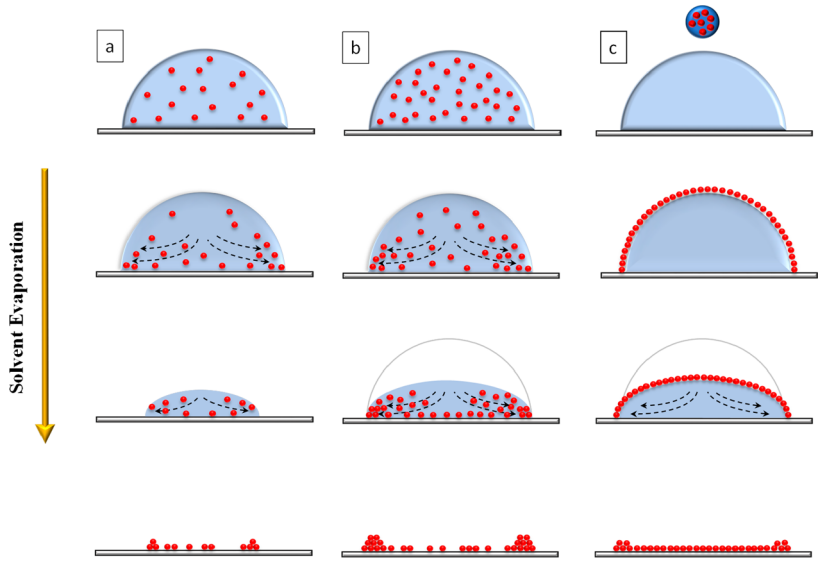

Figure 2. Schematics of conventional inkjet printing and dual-droplet inkjet printing of particle-laden droplets. (a) Conventional inkjet printing of sessile droplet with low particle loading that depicts the depinning/pinning behavior of the contact line. (b) Conventional inkjet printing of particle-laden droplets with high particle loading. The particles migrate and concentrate at the contact line by virtue of the evaporation-induced flow, causing the contact-line pinning. (c) Dual-droplet printing process, where the contact lines remain pinned during solvent evaporation. The middle of the deposit is composed of a nearly closely packed monolayer of nanoparticles.

particle concentration is increased to 5 mg/mL. The increase in particle size decreases the crack density obtained in the formed rings. Nevertheless, all 100 and 20 nm PS particles experience the coffee-ring formation in their deposits, through either initial particle pinning (20 nm with 5 mg/mL particle concentration) or secondary particle pinning (all other cases). A further increase in particle size (e.g., 1 μm PS particles) generated different outcomes. The biggest difference is the failure of the secondary pinning in the later stages of solvent evaporation. Low particle concentration (i.e., 0.2 mg/mL) yields irregular patterns due to the low number of particles, which, in turn, results in weak particle−substrate interactions. At 3 mg/mL particle concentration, the depinning/pinning behavior is observed, whereas at higher particle concentration (i.e., 5 mg/mL), the particles pinning at the initial contact line are sustained. For both cases, however, as the evaporation process proceeds, the solvent depins from the initially formed or the secondary contact lines, sweeping most of the colloidal particles toward the center of the deposit. Unlike smaller particles (i.e., 20 and 100 nm carboxyl-PS particles), most of the 1 μm PS particles do not get sufficient time to transport to the contact line before the contact line recedes. Instead, they are swept by the depinned receding contact line and lumped in the middle of the deposit. In other words, for very dilute colloidal suspensions of the 1 μm particles, the number of particles is insufficient to pin the solvent contact line. As a result, no coffee-ring formation occurs for the 1 μm PS particles. Figure 2a,b illustrates the particle assembly in conventional particle-laden droplets with a moderate receding contact angle.

Very recently, we have successfully demonstrated a nearly monolayer, closely packed deposition of colloidal nanoparticles through a dual-droplet inkjet printing process. Nanoparticle-laden wetting droplets were jetted over a supporting droplet, which was first deposited. Regulating surface tensions, droplet speeds, and droplet volumes resulted in effective particle spreading over the interface of the supporting droplet. The dynamics of wetting droplet impacting the supporting droplet, spreading of nanoparticles, and solvent evaporation were discussed in detail in our previous report.[39] Different from the conventional direct inkjet printing process, the dual-droplet inkjet printing offers an alternative concept for particle pinning at the contact line. Figure 2 demonstrates the difference in contact-line pinning mechanisms between the dual-droplet inkjet printing and conventional inkjet printing processes. Upon the initial impact of the wetting droplet on the interface of the supporting droplet, the sulfate-PS nanoparticles spread at the air−liquid interface under the influence of Marangoni flow established by ethanol/water surface tension gradient. Consequently, the colloidal PS nanoparticles agglomerate and self-assemble at the interface driven by capillary forces (i.e., particle−particle interactions) to likely form monolayer networks of nanoparticles.[39,40] These particle networks remain arrested at the air−liquid interface of the supporting droplet in an energetically favorable state due to the interfacial deformation caused by the fractal shape of the floating particle networks.[41] As the floating particles along the air−liquid interface reach the substrate, van der Waals and electrostatic interactions between the particles and the substrate become the driving forces for pinning the particles at the contact-line region. Thus the particle coverage at the air−liquid interface affects the particle pinning at the contact line, which influences the deposition structure through the interfacial self-assembly. Figure S2 shows the particle deposits produced by jetting wetting droplets with the 300 nm sulfate-PS particles on supporting droplets contain water only. Partial pinning occurs when insufficient particles present at the interface, where the self-assembled "islands" deposit preferably to a region with perfect solvent pinning at the contact line. Nearly full coverage at the interface may cause either holey deposition of the particles and good particle pinning at the contact line or locally depinned deposition at the contact line and closely packed structure within the deposition. A full coverage with a slight surplus of the floating particles at the interface facilitates the particle pinning at the contact line.

DOI: 10.1021/acs.langmuir.8b03406
Langmuir 2019, 35, 2209−2220

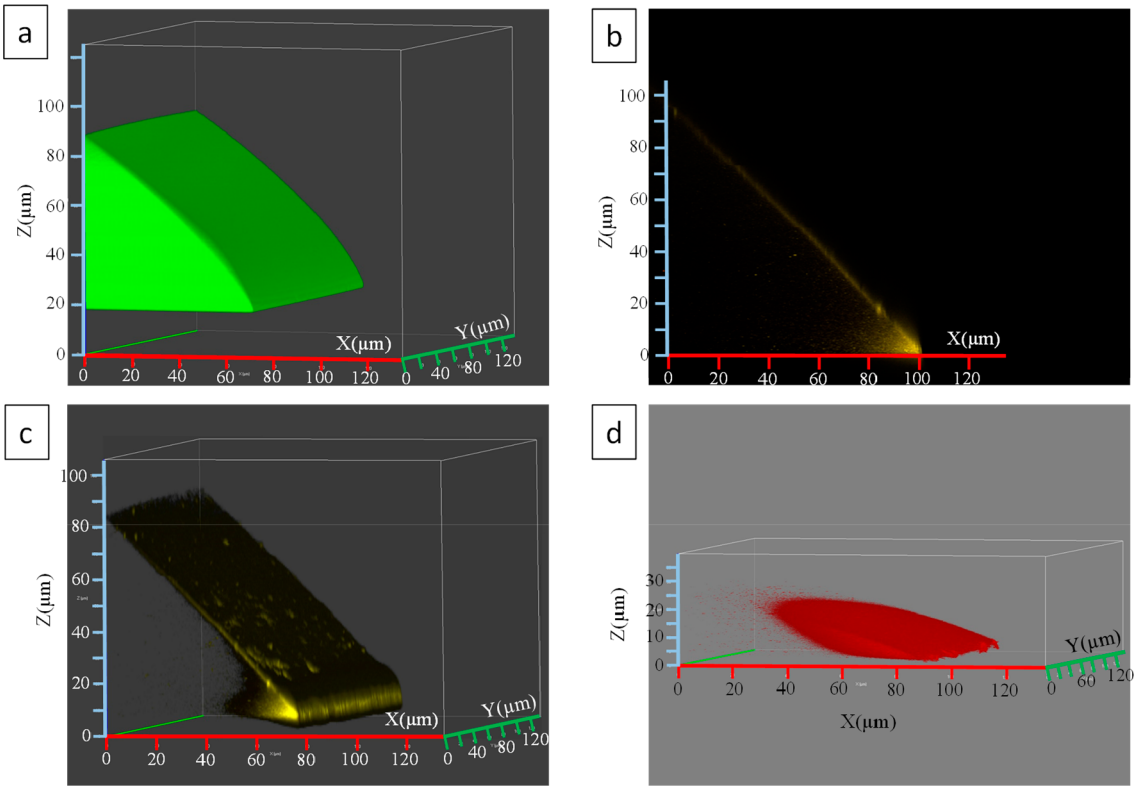

Figure 3. Confocal microscope images of (a) a supporting droplet of DI water on a coverslip glass slide with no particles in the bulk and at the air–liquid interface, (b,c) 200 nm sulfate-PS particles self-assembled at the interface of the supporting droplet and particle pinning at the contact line, and (d) 20 nm carboxyl-PS particle transporting to the contact line of the supporting droplet.

As illustrated in Figure 2c, the particles transport toward the substrate along the air–liquid interface of the supporting droplet, causing the particle pinning at the contact line as a result of particle–substrate interactions. This particle pinning mechanism from the air–liquid interface is insensitive to the receding contact angle, unlike the conventional contact-line pinning of sessile droplets. Such pinning process is highly dependent on particle concentration and particle size based on the premise that the particles successfully self-assemble into floating networks at the interface.

At high enough particle concentration (e.g., seven wetting droplets, with individual droplet size of ~550 pL, which corresponds to a particle concentration of 2.98×10^6 particle/mm^2), the particle pinning at the contact line was achieved. However, this particular particle number density is not sufficient to cover the entire interface of the supporting droplet. For this reason, higher particle number density (i.e., nine wetting droplets that correspond to particle concentration of 3.83×10^6 particle/mm^2) is needed to pin the particles at the contact line and give a complete coverage of nanoparticles at the interface. In this case, once the sulfate-PS particles reach the contact line, the capillary force initiated by solvent evaporation and the impeded receding contact line could not fold the near-monolayer of particles assembled at the air–liquid interface, and the contact line remained pinned during the evaporation process. On the contrary, depinning of the contact line was observed when fewer than seven wetting droplets were used (Figure S2). This could be attributed to the insufficient number of nanoparticles that reached the contact line, which, in turn, resulted in weak particle–substrate interactions. On the basis of this observation, nine wetting droplets were used in the following binary particle deposition, which corresponds to 3.83×10^6 particle/mm^2. It is worth pointing out that the ring formed at the contact line is a result of the evaporation-induced flow at the interface and particle–substrate interactions in the contact-line region (e.g., electrostatic and van der Waals interactions). In particular, during last stages of solvent evaporation, the particles at the interface may experience a "rush hour" effect.[42] This ring formation can be mitigated or suppressed by adjusting the pH of the supporting droplet and the particle–substrate interactions.[40] In other words, the particle pinning at the contact line still occurs even without the ring structure in this dual-droplet configuration.

Confocal Imaging of Particle Pinning at the Contact Line. Direct imaging of particle pinning at the contact line from the particles at the interface of the supporting droplet and those in the bulk of the supporting droplet was obtained using 3D confocal microscopy. Figure 3a presents a confocal image of a 110 μL water droplet with 0.1 mg/mL concentration of fluorescein F-1300 on a coverslip glass slide. This is meant to represent the supporting droplet and the air–liquid interface with no particles in the bulk or floating at the interface of the supporting droplet. Careful dispensing of sulfate-PS particles (5 μL) on the interface of the supporting droplet (water only) resulted in spreading of nanoparticles at the air–liquid interface. Figure 3b,c shows side-view and three-dimensionally stacked images of the same supporting droplet that clearly confirm the film formation of nanoparticles at the interface of the supporting droplet. Figure 3d, on the contrary, shows the 20 nm carboxyl-PS nanoparticles circulating in the bulk of the supporting droplet, where the particles transport and concentrate at the contact-line region empowered by the evaporation-induced flow. To avoid the crosstalk between the fluorescent dyes of nanoparticles, imaging of the 20 nm

DOI: 10.1021/acs.langmuir.8b03406
Langmuir 2019, 35, 2209–2220

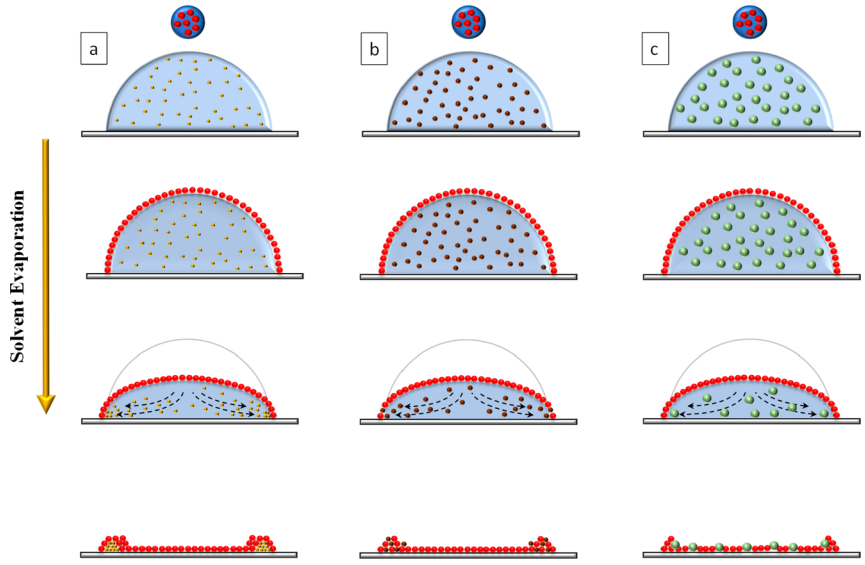

Figure 4. Schematic of dual-droplet inkjet printing that demonstrates the monolayer formation of nanoparticles at the interface (300 nm sulfate-PS) and different particle assembly obtained near the three-phase contact line depending on the particle size in the supporting droplet: (a) 20 nm carboxyl-PS particles forming the stratified ring structure, (b) 100 nm carboxyl-PS particles resulting in the blended ring structure, and (c) 1 μm carboxyl-PS particles leading to a scattered particle deposition among the particle assembly from the interface.

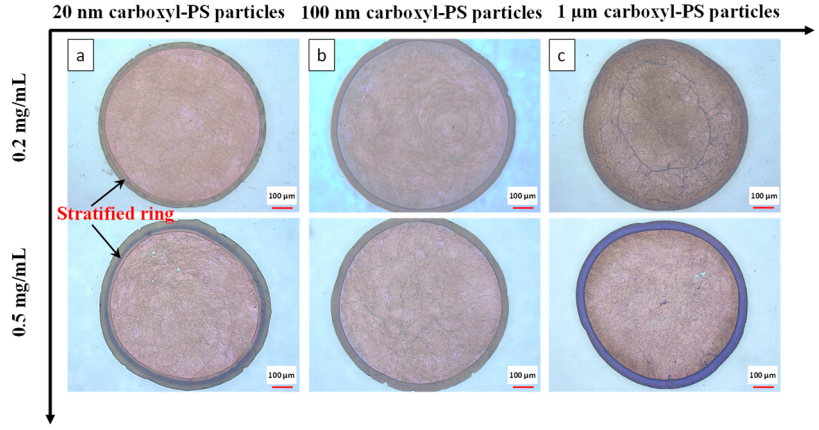

Figure 5. Optical images of the particle depositions generated by dual-droplet printing of nine wetting droplets with 300 nm sulfate-PS particles and different sizes and concentrations of carboxyl-PS particles in the supporting droplet: (a) 20 nm carboxyl-PS particles, (b) 100 nm carboxyl-PS particles, and (c) 1 μm carboxyl-PS particles. The scale bar is 100 μm.

carboxyl-PS particles in the bulk and the 200 nm sulfate-PS particles on the interface of the supporting droplet was carried out separately. It should be mentioned that the images shown in Figure 3b,c were taken right after dispensing the colloidal particles on the surface of the supporting droplet. The particles at the interface get pinned at the contact lines of the supporting droplet quickly after the wetting droplet spreading. However, for the colloidal particles in the supporting droplet only (Figure 3d), the 3D image was taken at ~30 min after dispensing the droplet, which was selected to demonstrate a clear particle pinning and coffee-ring formation at the contact line of the supporting droplet. The 3D image represents the average particle motion captured within the ~15 min scanning interval elapsed between the first and last scanned slices (30 μm z-height distance). However, this is not a concern for particles assembled at the interface of the supporting droplet because the particle networks are very robust at the interface until the final stages of solvent evaporation.

Binary Particle Deposition in Dual-Droplet Printing. In this study, we investigate the particle pinning and accumulation near the contact lines by introducing nanoparticles into both the wetting droplet and the supporting droplet through dual-droplet printing. The supporting droplet was generated by multiple bursts of inkjet droplets that were equivalent to ~110 nL of DI water with carboxyl-PS particles. Nine wetting droplets with sulfate-PS particles (single droplet volume of ~550 pL) were deposited onto the supporting droplet by a secondary printhead. In all of the experiments, the modified Weber number (We') was controlled below 0.42 to ensure the spreading of the wetting droplet over the surface of the supporting one.[39,43] The objective of this study is to examine the particle arrangement in the contact-line region initiated by the self-assembled particles from the air−liquid interface and its competition against particles transported from the bulk of the supporting droplet to the three-phase contact line.

DOI: 10.1021/acs.langmuir.8b03406
Langmuir 2019, 35, 2209−2220

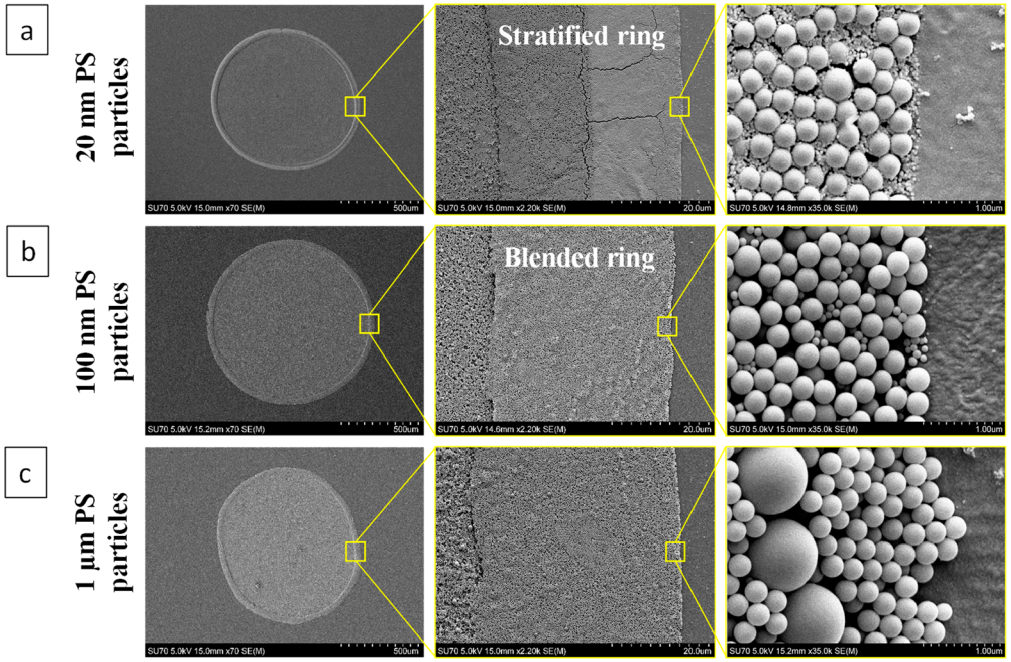

Figure 6. SEM images of the particle deposits shown in Figure 5, demonstrating the versatile particle assembly obtained in vicinity of the contact-line region: (a) stratified ring (20 nm carboxyl-PS particles), (b) blended ring (100 nm carboxyl-PS particles), and (c) ring of 300 nm sulfate-PS particles decorated with a few 1 μm carboxyl-PS particles. Carboxyl-PS nanoparticles of 0.2 mg/mL were used in the supporting droplet.

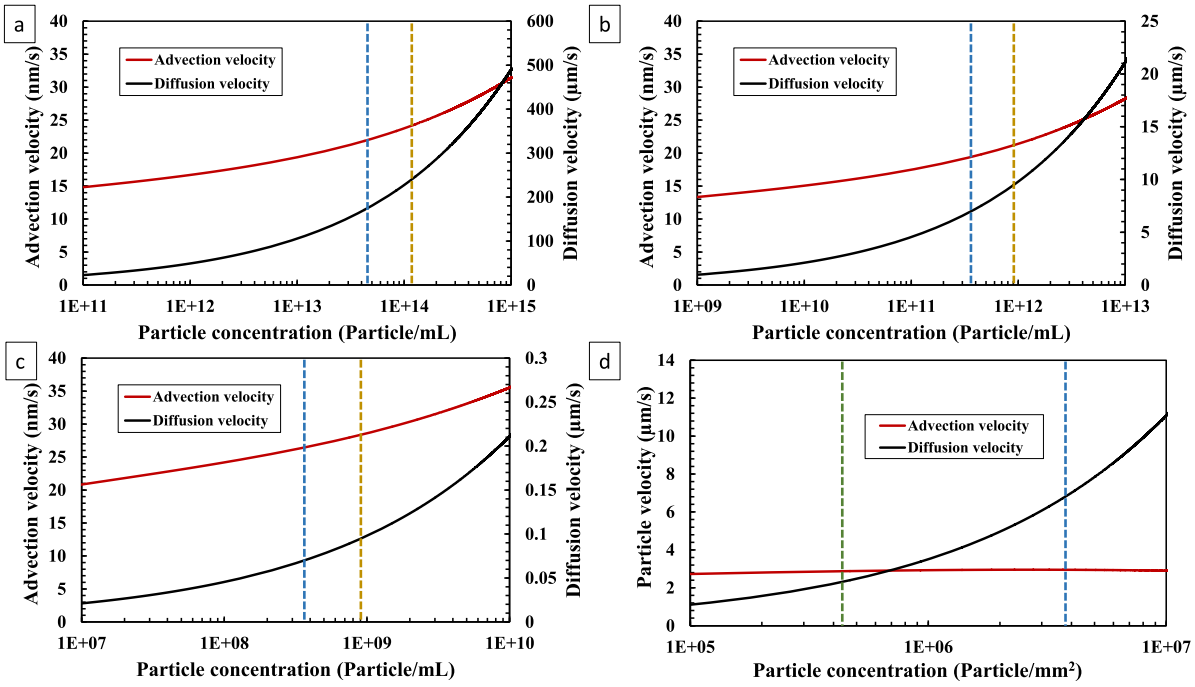

Figure 7. (a–c) Calculated advection and diffusion velocities of the 20 nm, 100 nm, and 1 μm carboxyl-PS particles in the bulk of the supporting droplet, respectively. The dashed lines represent 0.2 and 0.5 mg/mL particle concentrations used in the experimental study. (d) Calculated advection and diffusion velocities of the 300 nm sulfate-PS particles at the interface of the supporting droplet. The dashed lines represent the range of particle concentrations obtained from jetting one to nine wetting droplets.

Figure 4 illustrates the different particle deposition obtained in dual-droplet inkjet printing with respect to different particle sizes in the supporting droplet. Smaller particles (i.e., the 20 nm carboxyl-PS particles) in the bulk of the supporting droplet tend to exclusively transport and deposit to construct the outermost ring of the supporting droplet, whereas particles coming from the interface (i.e., the 300 nm sulfate-PS particles) of the supporting droplet tend to concentrate in the inner region surrounded by the 20 nm particles forming a stratified ring deposition (Figure 4a).

Utilizing bigger particle size in the supporting droplet (i.e., 100 nm carboxyl-PS particles) results in a similar behavior, where the particles transport to the contact-line region. However, the 100 nm carboxyl-PS particles mix with the 300

DOI: 10.1021/acs.langmuir.8b03406
Langmuir 2019, 35, 2209–2220

nm sulfate-PS particles at the contact-line region, forming a blended ring structure (Figure 4b). Contrary to the 20 and 100 nm PS particles, not all of the bigger particles in the bulk of the supporting droplet (i.e., 1 μm carboxyl-PS particles) transport to the three-phase contact-line region by the evaporation-induced flow. Instead, the 1 μm carboxyl-PS particles are scattered throughout the deposition footprint (Figure 4c). In this case, the ring in such deposits is mainly composed of particles coming from the interface decorated with a few 1 μm carboxyl-PS particles coming from the bulk. (More information is provided in the following section.)

Figure 5 presents optical images of particle depositions generated via a dual-droplet inkjet printing process with different carboxyl-PS particle sizes and concentrations in the bulk of the supporting droplet. The red color shown in the middle of each particle deposition indicates the monolayer formation of nanoparticles obtained by jetting nine wetting droplets over the supporting droplet. Figure 6 and Figures S3–S6 demonstrate the particle assembly obtained at the contact-line region using different carboxyl-PS particle sizes and concentrations in the bulk of the supporting droplet.

The ring width is influenced by the higher concentration of carboxyl-PS particles in the supporting droplet (Figure 5 and Figure S6). Specifically, the ring becomes wider for the 20 nm particles, which is attributed to the increased number of particles in the contact-line region. The 1 μm particles are covered by the monolayer assembly of the particles from the interface during solvent evaporation, which likely "fall off" those 1 μm particles due to capillary forces by their neighboring particles (Figure S5). This pushes more 300 nm sulfate-PS particles to the contact-line region, especially for the high concentration of carboxyl-PS particles.

Discussion. To get a better understanding of binary particles arrangement in the contact-line region produced by dual-droplet inkjet printing, the Hu–Larson model was implemented in this study.[27] Particle velocity, a combination of advection and diffusion velocities, is calculated near the contact line of the supporting droplet at the specified $\check{r}$ and vertical locations. Figure 7 shows the advection and diffusion velocities, calculated by eqs 4 and 5, respectively, for the particles in the bulk and at the interface of the supporting droplet approximated at the initial contact angle. The advection velocities calculated at various vertical locations are provided in Figure S7. On the contrary, the advection velocity of particles spread on the interface of the supporting droplet (i.e., sulfate-PS particles) was evaluated at the air–liquid interface only.

The experimental findings suggest that smaller particles transport at a faster pace to the contact line. This observation is verified by the calculated advection and diffusion particle velocities, as shown in Figure 7. For smaller particles (i.e., 20 and 100 nm particles), diffusion velocity dominates over the advection velocity. As the particle concentration further increases, both the diffusion and the advection velocities increase. According to eq 4, the increase in diffusion velocity is attributed to the incremental decrease in the mean distance between two colloidal particles with respect to higher particle concentration. The advection velocity is comparable for the various particle sizes used in this work. The calculated advection velocity is the velocity of the evaporation-induced flow. For different particle sizes, the evaporation-induced flow is the same, but the advection velocities are calculated at different locations. On the contrary, the diffusion velocity decreases up to three orders of magnitude for larger particles, for example, from a few hundred microns per second for 20 nm particles to a fraction of a micron per second for 1 μm particles. By comparing the advection and diffusion velocities of colloidal particles, it is evident that the 20 nm carboxyl-PS particles have the highest particle velocity among their counterparts, which renders the particle pinning outside the 300 nm particle assembly.

To generalize the findings and construct the phase diagram of particle deposition, especially in the contact-line region, we further calculated the characteristic time for particle pinning from the bulk of the supporting droplet (t_{ps}), the characteristic time for the particles at the interface to reach the contact line (t_{pw}), and the total time for solvent evaporation (t_{evp}) for various particle sizes and particle concentrations. Figure 8

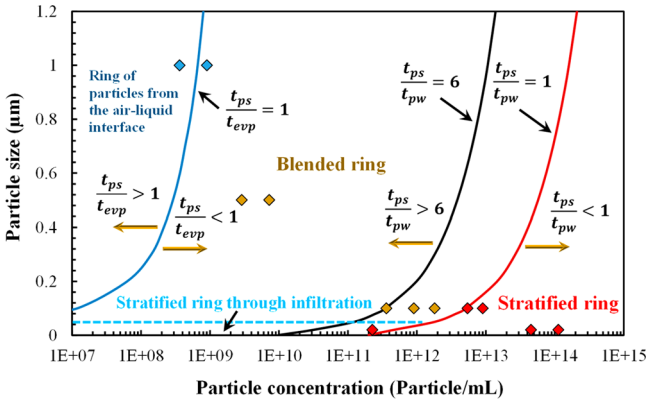

Figure 8. Phase diagram of the deposition morphology showing its dependence on the particle size and concentration in the supporting droplet. Diamond dots indicate the experimental data. Different dot colors correspond to different ring structures.

manifests the competition among the solvent evaporation, particle pinning from the bulk, and particle pinning from the interface of the supporting droplet. Specifically, the characteristic time ratio t_{ps}/t_{evp} determines if the particles from the bulk of the supporting droplet can reach the contact line before solvent evaporation completes; the characteristic time ratio t_{ps}/t_{pw} evaluates the competition between the particle pinning from the bulk and at the interface of the supporting droplet. When the characteristic time ratio $t_{ps}/t_{evp} > 1$, this implies that solvent evaporation is relatively faster than the time required for the particles to reach the contact line, resulting in the suppression of the ring formation of colloidal particles at the edge of the supporting droplet. Yet $t_{ps}/t_{evp} \ll 1$ indicates that the colloidal particles reach the contact line before the completion of the solvent evaporation, facilitating the ring formation of particles from the bulk of the supporting droplet. In addition, for $t_{ps}/t_{pw} < 1$, the colloidal particles in the supporting droplet reach and deposit near the contact line faster than those at the interface of the supporting droplet, forming a stratified ring structure. On the contrary, $t_{ps}/t_{pw} \gg 1$ describes the fast arrival and pinning of the interface floating particles to the contact line compared with those dispersed in the bulk of the supporting droplet, producing either the mixed ring structure or a ring that is mainly composed of particles from the interface with scattered particles from the bulk of the supporting droplet. It is worth pointing out that t_{pw}/t_{evp} is much smaller than one (3.32×10^{-4}) in the current dual-droplet configuration, indicating that the particles at the

DOI: 10.1021/acs.langmuir.8b03406
Langmuir 2019, 35, 2209–2220

interface reach and pin at the contact line much faster than the solvent evaporation.

The calculated characteristic times and ratios are listed in the Supporting Information (Table S1). In the case of using the 20 nm carboxyl-PS particles in the bulk and 300 nm sulfate-PS particles at the air−liquid interface, the characteristic time ratios $t_{ps}/t_{evp} \ll 1$ and $t_{ps}/t_{pw} \ll 1$ are obtained for the 0.2 and 0.5 mg/mL particle concentrations. This indicates that the 20 nm PS particles reach and deposit near the contact lines faster than the 300 nm PS particles, producing particle deposition with a stratified ring structure. All 20 nm PS particles have been observed to migrate to the contact-line region, leaving the middle of the deposit only a monolayer of the 300 nm PS particles (Figure 6a and Figure S3). This is different from the shrunk ring structure shown in Figure 1a under the same particle concentration. One possible explanation is that some 300 nm PS particles pin at the contact lines, effectively anchor the solvent contact line, prevent sweeping the 20 nm particles back to the center, and facilitate the pinning of the 20 nm particles (Figure S8). During the last stage of solvent evaporation, some 300 nm PS particles get accumulated at the contact lines and delaminated from the first ring of the 20 nm PS particles, forming the stratified ring structures. It is worth pointing out that when the 300 nm particles pin at the contact line, the 20 nm particles might still infiltrate through the 300 nm particles through the interstices, forming a stratified ring structure. Figure S9 shows the stratified ring structure obtained when 20 nm particles with solid concentration of 0.001 mg/mL are used in the supporting droplet. Therefore, a dashed line is added to the diagram as an infiltration threshold (46.4 nm), which corresponds to the maximum particle size fitting into the interstices of closely packed 300 nm particles. Underneath the dashed line, particle infiltration may occur, leading to stratified ring structures. When $t_{ps}/t_{pw} \ll 1$, for small particles, the stratified ring formation could be attributed to both the fast particle pinning and the particle infiltration.

Changing the particle size in the bulk of the supporting droplet to 100 nm along with the 300 nm sulfate-PS particles at the interface has led to a different scenario. In this case, for particle concentrations of 0.2 and 0.5 mg/mL, the characteristic time ratios become $t_{ps}/t_{evp} \ll 1$ and $t_{ps}/t_{pw} \approx 3-6$, which correspond to the blended ring structure. Figure 6b and Figure S4 display the particle deposition of 100 nm carboxyl-PS particles in the bulk and 300 nm sulfate-PS particles at the interface of the supporting droplet, respectively. In a similar fashion, the majority of the 100 nm PS particles are transported to the contact-line region; however, the ring produced is a blend of particles from the bulk and particles at the air−liquid interface. To validate the analytical model, higher concentrations of 100 nm particles, that is, 1, 3, and 5 mg/mL, were tested, and the deposition morphology is shown in Figure S10. The stratified ring structure in the cases of 3 and 5 mg/mL becomes more obvious, whereas the deposition of 1 mg/mL shows the transition from blended ring structure to stratified ring structure.

The characteristic time ratios became $t_{ps}/t_{evp} \approx 1$ and $t_{ps}/t_{pw} \gg 1$ when the 1 μm PS particles (0.2 mg/mL) were utilized in the bulk of the supporting droplet. Accordingly, the particles could not reach and pin at the contact line of the supporting droplet as the solvent was evaporated. Instead, the 1 μm PS particles are scattered throughout the deposit, and no particle accumulation forms at the three-phase contact line, which is consistent with the experimental results (Figure 6c and Figure S5). The contact-line pinning in this case occurs only by the contribution of particles from the air−liquid interface. In addition, 500 nm carboxyl-PS particles with solid concentrations of 0.2 and 0.5 mg/mL were used to generate the blended ring structures (Figure S11), which agree with the model prediction.

It is worth noting that the boundaries between the stratified ring, blended ring, and the ring of particles formed from the air−liquid interface are not absolutely sharp. We have noticed that the majority of the 100 nm PS particles deposit in the contact-line region, forming the blended rings with the 300 nm PS particles, however, there is a trace amount of particles deposited in the middle of the self-assembled 300 nm PS film (Figure S4). Nevertheless, this phase diagram provides valuable information for understanding the effect of particle pinning on the assembly structures of binary particles in evaporative droplets.

CONCLUSIONS

In this study, two mechanisms of particle pinning at the contact lines, that is, pinning from the bulk of a sessile droplet and pinning from the interface of a sessile droplet, have been investigated through the dual-droplet inkjet printing. The competition of these two mechanisms has been systematically studied by introducing PS particles to the wetting droplet and the supporting droplet. Depending on the particle size and the concentration of the particles dispersed in the bulk of the supporting droplet, versatile particle arrangements near the contact line such as stratified rings, blended rings, and rings with particles mainly from the air−liquid interface have been obtained. An analytical analysis was conducted using the Hu−Larson model to understand the binary particle arrangement near the contact line of the supporting droplet. It qualitatively agrees well with the experimental results. For small nanoparticles such as 20 nm carboxyl-PS particles in the bulk and 300 nm sulfate-PS particles at the air−liquid interface, the calculated characteristic time ratios are $t_{ps}/t_{evp} \ll 1$ and $t_{ps}/t_{pw} \ll 1$, which suggest the stratified ring formation due to the fast movement of the carboxyl-PS particles toward the contact line as compared with the particles at the air−liquid interface, whereas particle infiltration through the interstitial space of the 300 nm particles may also contribute to the stratified ring formation. Changing the particle size in the bulk of the supporting droplet to 100 nm with moderate concentrations results in blended rings due to the comparable particle size and particle velocities in the system. On the contrary, the characteristic time ratios become $t_{ps}/t_{evp} \approx 1$ and $t_{ps}/t_{pw} \gg 1$ when the 1 μm PS particles are utilized in the bulk of the supporting droplet. For such big colloidal particles, the evaporation-induced flow and particle diffusion are insufficient to drive the particles to the rim of the supporting droplet. As a result, the 1 μm PS particles are scattered throughout the deposit, and the contact lines are pinned by the particles mainly from the air−liquid interface. Understanding the transport mechanism of colloidal particles and controlling the deposition assembly from the bulk and at the interface of sessile droplets could potentially lead to a new strategy for producing functional coatings and devices.

DOI: 10.1021/acs.langmuir.8b03406
Langmuir 2019, 35, 2209−2220

■ ASSOCIATED CONTENT

Supporting Information

The Supporting Information is available free of charge on the ACS Publications website at DOI: 10.1021/acs.langmuir.8b03406.

Schematics of the particles at the contact line. Optical images of particle deposition of the dual-droplet printing with various numbers of wetting droplets. SEM images of the binary particle assembly with the stratified ring structure, blended ring structure, and rings composed of particles mainly from the interface of the supporting droplet. Radial velocity at ten equally spaced vertical heights between the substrate and the interface. Further illustration of the formation of stratified ring structure. Stratified ring structure formed by infiltration through the interparticle interstices. Transition from blended ring structure to stratified ring structure. More blended ring structures for validation of the phase diagram. Calculated characteristic times and ratios (PDF)

■ AUTHOR INFORMATION

Corresponding Author

*E-mail: hzhao2@vcu.edu. Tel: (804) 827-7025. Fax: (804) 827-7030.

ORCID

Hong Zhao: 0000-0001-9148-0158

Notes

The authors declare no competing financial interest.

■ ACKNOWLEDGMENTS

We are grateful for the support of the National Science Foundation (CMMI-1634938).

■ REFERENCES

(1) Sun, J.; Bao, B.; He, M.; Zhou, H.; Song, Y. Recent Advances in Controlling the Depositing Morphologies of Inkjet Droplets. *ACS Appl. Mater. Interfaces* **2015**, *7* (51), 28086−28099.

(2) Anyfantakis, M.; Baigl, D. Manipulating the Coffee-Ring Effect: Interactions at Work. *ChemPhysChem* **2015**, *16* (13), 2726−2734.

(3) Han, W.; Lin, Z. Learning from "Coffee Rings": Ordered Structures Enabled by Controlled Evaporative Self-Assembly. *Angew. Chem., Int. Ed.* **2012**, *51* (7), 1534−1546.

(4) Sempels, W.; De Dier, R.; Mizuno, H.; Hofkens, J.; Vermant, J. Auto-Production of Biosurfactants Reverses the Coffee Ring Effect in a Bacterial System. *Nat. Commun.* **2013**, *4*, 1757.

(5) Shen, X.; Ho, C. M.; Wong, T. S. Minimal Size of Coffee Ring Structure. *J. Phys. Chem. B* **2010**, *114* (16), 5269−5274.

(6) Dugyala, V. R.; Basavaraj, M. G. Control over Coffee-Ring Formation in Evaporating Liquid Drops Containing Ellipsoids. *Langmuir* **2014**, *30* (29), 8680−8686.

(7) Yunker, P. J.; Still, T.; Lohr, M. A.; Yodh, A. G. Suppression of the Coffee-Ring Effect by Shape-Dependent Capillary Interactions. *Nature* **2011**, *476* (7360), 308−311.

(8) Lin, S. Y.; Yang, K. C.; Chen, L. J. Effect of Surface Hydrophobicity on Critical Pinning Concentration of Nanoparticles to Trigger the Coffee Ring Formation during the Evaporation Process of Sessile Drops of Nanofluids. *J. Phys. Chem. C* **2015**, *119* (6), 3050−3059.

(9) Bhardwaj, R.; Fang, X.; Somasundaran, P.; Attinger, D. Self-Assembly of Colloidal Particles from Evaporating Droplets: Role of DLVO Interactions and Proposition of a Phase Diagram. *Langmuir* **2010**, *26* (11), 7833−7842.

(10) Devineau, S.; Anyfantakis, M.; Marichal, L.; Kiger, L.; Morel, M.; Rudiuk, S.; Baigl, D. Protein Adsorption and Reorganization on Nanoparticles Probed by the Coffee-Ring Effect: Application to Single Point Mutation Detection. *J. Am. Chem. Soc.* **2016**, *138* (36), 11623−11632.

(11) Parsa, M.; Harmand, S.; Sefiane, K.; Bigerelle, M.; Deltombe, R. Effect of Substrate Temperature on Pattern Formation of Nanoparticles from Volatile Drops. *Langmuir* **2015**, *31* (11), 3354−3367.

(12) Li, Y. F.; Sheng, Y. J.; Tsao, H. K. Evaporation Stains: Suppressing the Coffee-Ring Effect by Contact Angle Hysteresis. *Langmuir* **2013**, *29* (25), 7802−7811.

(13) Deegan, R. D. Pattern Formation in Drying Drops. *Phys. Rev. E: Stat. Phys., Plasmas, Fluids, Relat. Interdiscip. Top.* **2000**, *61* (1), 475−485.

(14) Deegan, R. D.; Bakajin, O.; Dupont, T. F.; Huber, G.; Nagel, S. R.; Witten, T. A. Capillary Flow as the Cause of Ring Stains from Dried Liquid Drops. *Nature* **1997**, *389* (6653), 827−829.

(15) Gençer, A.; Schütz, C.; Thielemans, W. Influence of the Particle Concentration and Marangoni Flow on the Formation of Cellulose Nanocrystal Films. *Langmuir* **2017**, *33* (1), 228−234.

(16) He, P.; Derby, B. Controlling Coffee Ring Formation during Drying of Inkjet Printed 2D Inks. *Adv. Mater. Interfaces* **2017**, *4* (22), 1700944.

(17) Talbot, E. L.; Yow, H. N.; Yang, L.; Berson, A.; Biggs, S. R.; Bain, C. D. Printing Small Dots from Large Drops. *ACS Appl. Mater. Interfaces* **2015**, *7* (6), 3782−3790.

(18) Eom, D. S.; Chang, J.; Song, Y. W.; Lim, J. A.; Han, J. T.; Kim, H.; Cho, K. Coffee-Ring Structure from Dried Graphene Derivative Solutions: A Facile One-Step Fabrication Route for All Graphene-Based Transistors. *J. Phys. Chem. C* **2014**, *118* (46), 27081−27090.

(19) Li, Y.; Zhang, W.; Hu, J.; Wang, Y.; Feng, X.; Du, W.; Guo, M.; Liu, B. F. Rapid Assembly of Large Scale Transparent Circuit Arrays Using PDMS Nanofilm Shaped Coffee Ring. *Adv. Funct. Mater.* **2017**, *27* (11), 1606045.

(20) Layani, M.; Gruchko, M.; Milo, O.; Balberg, I.; Azulay, D.; Magdassi, S. Transparent Conductive Coatings by Printing Coffee Ring Arrays Obtained at Room Temperature. *ACS Nano* **2009**, *3* (11), 3537−3542.

(21) Monteux, C.; Lequeux, F. Packing and Sorting Colloids at the Contact Line of a Drying Drop. *Langmuir* **2011**, *27* (6), 2917−2922.

(22) Noguera-Marín, D.; Moraila-Martínez, C. L.; Cabrerizo-Vílchez, M. A.; Rodríguez-Valverde, M. A. Particle Segregation at Contact Lines of Evaporating Colloidal Drops: Influence of the Substrate Wettability and Particle Charge-Mass Ratio. *Langmuir* **2015**, *31* (24), 6632−6638.

(23) Wong, T. S.; Chen, T. H.; Shen, X.; Ho, C. M. Nanochromatography Driven by the Coffee Ring Effect. *Anal. Chem.* **2011**, *83* (6), 1871−1873.

(24) Hu, H.; Larson, R. G. Evaporation of a Sessile Droplet on a Substrate. *J. Phys. Chem. B* **2002**, *106* (6), 1334−1344.

(25) Einstein, A. *Investigations on the Theory of the Brownian Movement*; Dover Publications, Inc., 1956.

(26) Pack, M.; Hu, H.; Kim, D. O.; Yang, X.; Sun, Y. Colloidal Drop Deposition on Porous Substrates: Competition among Particle Motion, Evaporation, and Infiltration. *Langmuir* **2015**, *31* (29), 7953−7961.

(27) Hu, H.; Larson, R. G. Analysis of the Microfluid Flow in an Evaporating Sessile Droplet. *Langmuir* **2005**, *21* (9), 3963−3971.

(28) Bourgès-Monnier, C.; Shanahan, M. E. R. Influence of Evaporation on Contact Angle. *Langmuir* **1995**, *11* (7), 2820−2829.

(29) Christy, J. R. E.; Hamamoto, Y.; Sefiane, K. Flow Transition within an Evaporating Binary Mixture Sessile Drop. *Phys. Rev. Lett.* **2011**, *106* (20), 205701.

(30) Weon, B. M.; Je, J. H. Self-Pinning by Colloids Confined at a Contact Line. *Phys. Rev. Lett.* **2013**, *110* (2), No. 028303.

(31) Ma, H.; Hao, J. Ordered Patterns and Structures via Interfacial Self-Assembly: Superlattices, Honeycomb Structures and Coffee Rings. *Chem. Soc. Rev.* **2011**, *40* (11), 5457−5471.

(32) Morales, V. L.; Parlange, J. Y.; Wu, M.; Pérez-Reche, F. J.; Zhang, W.; Sang, W.; Steenhuis, T. S. Surfactant-Mediated Control of

DOI: 10.1021/acs.langmuir.8b03406
Langmuir 2019, 35, 2209−2220

Colloid Pattern Assembly and Attachment Strength in Evaporating Droplets. *Langmuir* **2013**, *29* (6), 1831−1840.
(33) Yan, Q.; Gao, L.; Sharma, V.; Chiang, Y. M.; Wong, C. C. Particle and Substrate Charge Effects on Colloidal Self-Assembly in a Sessile Drop. *Langmuir* **2008**, *24* (20), 11518−11522.
(34) Kim, D. O.; Pack, M.; Hu, H.; Kim, H.; Sun, Y. Deposition of Colloidal Drops Containing Ellipsoidal Particles: Competition between Capillary and Hydrodynamic Forces. *Langmuir* **2016**, *32* (45), 11899−11906.
(35) Jung, J. Y.; Kim, Y. W.; Yoo, J. Y.; Koo, J.; Kang, Y. T. Forces Acting on a Single Particle in an Evaporating Sessile Droplet on a Hydrophilic Surface. *Anal. Chem.* **2010**, *82* (3), 784−788.
(36) Chhasatia, V. H.; Sun, Y. Interaction of Bi-Dispersed Particles with Contact Line in an Evaporating Colloidal Drop. *Soft Matter* **2011**, *7* (21), 10135−10143.
(37) Routh, A. F. Drying of Thin Colloidal Films. *Rep. Prog. Phys.* **2013**, *76* (4), No. 046603.
(38) Anyfantakis, M.; Baigl, D.; Binks, B. P. Evaporation of Drops Containing Silica Nanoparticles of Varying Hydrophobicities: Exploiting Particle-Particle Interactions for Additive-Free Tunable Deposit Morphology. *Langmuir* **2017**, *33* (20), 5025−5036.
(39) Al-Milaji, K. N.; Secondo, R. R.; Ng, T. N.; Kinsey, N.; Zhao, H. Interfacial Self-Assembly of Colloidal Nanoparticles in Dual-Droplet Inkjet Printing. *Adv. Mater. Interfaces* **2018**, *5* (10), 1701561.
(40) Al-Milaji, K. N.; Radhakrishnan, V.; Kamerkar, P.; Zhao, H. pH-Modulated Self-Assembly of Colloidal Nanoparticles in a Dual-Droplet Inkjet Printing Process. *J. Colloid Interface Sci.* **2018**, *529*, 234−242.
(41) Loudet, J. C.; Yodh, A. G.; Pouligny, B. Wetting and Contact Lines of Micrometer-Sized Ellipsoids. *Phys. Rev. Lett.* **2006**, *97* (1), No. 018304.
(42) Zhao, M.; Yong, X. Nanoparticle Motion on the Surface of Drying Droplets. *Phys. Rev. Fluids* **2018**, *3* (3), No. 034201.
(43) Noda, Y.; Minemawari, H.; Matsui, H.; Yamada, T.; Arai, S.; Kajiya, T.; Doi, M.; Hasegawa, T. Underlying Mechanism of Inkjet Printing of Uniform Organic Semiconductor Films Through Antisolvent Crystallization. *Adv. Funct. Mater.* **2015**, *25* (26), 4022−4031.

DOI: 10.1021/acs.langmuir.8b03406
Langmuir 2019, 35, 2209−2220